Research paper

Bem2d.jl: A quadratic co-location two-dimensional boundary element approach to quasi-static faulting problems with gravity and non-planar topography

Brendan J. Meade [a,1,*], T. Ben Thompson [b,2]

[a] *Department of Earth and Planetary Sciences, Harvard University, Cambridge, MA, USA*
[b] *Medford, MA, USA*

ARTICLE INFO

ABSTRACT

Linear elastic boundary element models are commonly used tools to understand the mechanics of earthquake cycle processes and their contribution to the growth of tectonic structures. Here we describe a two-dimensional plane strain linear elastic boundary element approach to earthquake cycle and tectonic processes based on the displacement discontinuity method. This approach integrates an analytic solution for coincident interactions using three node quadratic elements and the classic particular integral approach to uni-directional gravity. Three node quadratic elements are more accurate than classical constant displacement elements and enable the exact representation displacements, stresses and tractions on elements subject to slip gradients. We demonstrate the recovery of analytic solutions and illustrate the combined effects of faulting and gravitational body forces in the presence of topographic relief.

1. Introduction

The earth's upper crust is frequently represented as a linear elastic medium over relatively short time scales (<1000 years). Boundary element models (BEMs) are a type of numerical model that can be used to represent interactions between fault slip, variations is material properties, topographic relief, and gravitational forcing in the presence of complex model geometry and require only boundary discretizations. ThisThe results from the fact that the boundary element solution can be represented as the superposition of analytic Greens functions (e.g., Comninou, 1973; Brown, 1975; Okada, 1985, 1992; Jeyakumaran et al., 1992; Thomas, 1993; Meade, 2007; Nikkhoo and Walter, 2015). These fundamental solutions for homogeneous full- and half-space geometries have been used for the kinematic imaging of fault activity across the earthquake cycle (e.g., Fialko et al., 2005; Pritchard et al., 2002; Vigny et al., 2005; Bilham et al., 1997; Bendick et al., 2000; Burgmann et al., 2002; Dixon et al., 2003; Dragert et al., 2001; Fukuda et al., 2008; Heki et al., 1997; Hirose et al., 1999; Maerten et al., 2005; McCaffrey, 1992; Murray et al., 2001; Ozawa et al., 2011; Johnson and Tebo, 2018; Johnson, 2018; Segall, 2010) and for quasi-dynamic earthquake cycle sequences (e.g., Erickson et al., 2019; Dieterich, 1992; Dieterich and Smith, 2009; Liu and Rice, 2005; Liu, 2013; Li and Liu, 2017; Wei et al., 2013).

Linear elastic problems with more complex geometries (e.g., non-planar topography, material property variations) and mixed (displacement, displacement discontinuity/fault slip, traction) boundary conditions can still be solved using boundary-only discretizations using general boundary element formulations (e.g., Banerjee and Butterfield, 1981; Crouch and Starfield, 1983; Brebbia and Dominguez, 1994; Gaul et al., 2013). In the field of earthquake and tectonic problems these have been used in both quasi static fault problems (e.g., Martel and Muller, 2000; Moon et al., 2017) as well as for geometrically complex faulting earthquake cycle models with topography and a mix of elastic and viscoelastic regions (Johnson and Tebo, 2018).

Here we describe an implementation (https://github.com/brendanjmeade/Bem2d.jl) of a two-dimensional plane strain linear elastic boundary element model that combines the accuracy of three node quadratic elements (e.g., Portela et al., 1992) and the particular integral method for unidirectional gravity (Pape and Banerjee, 1987) with a co-location approach (e.g., Crouch and Starfield, 1983). We demonstrate accuracy by approximating known analytic solutions and show how the methods implemented in Bem2d.jl can be used to construct solutions to tectonic problems that combine faulting, finite-domains, gravity, and non-planar topographic relief.

---

* Corresponding author.
  E-mail address: meade@fas.harvard.edu (B.J. Meade).
[1] BJM carried out the integration for the quadratic elements, wrote the code and the manuscript.
[2] TBT conceived of the analytic quadratic approach, provided guidance and direction and helped with the finalizing of the manuscript.
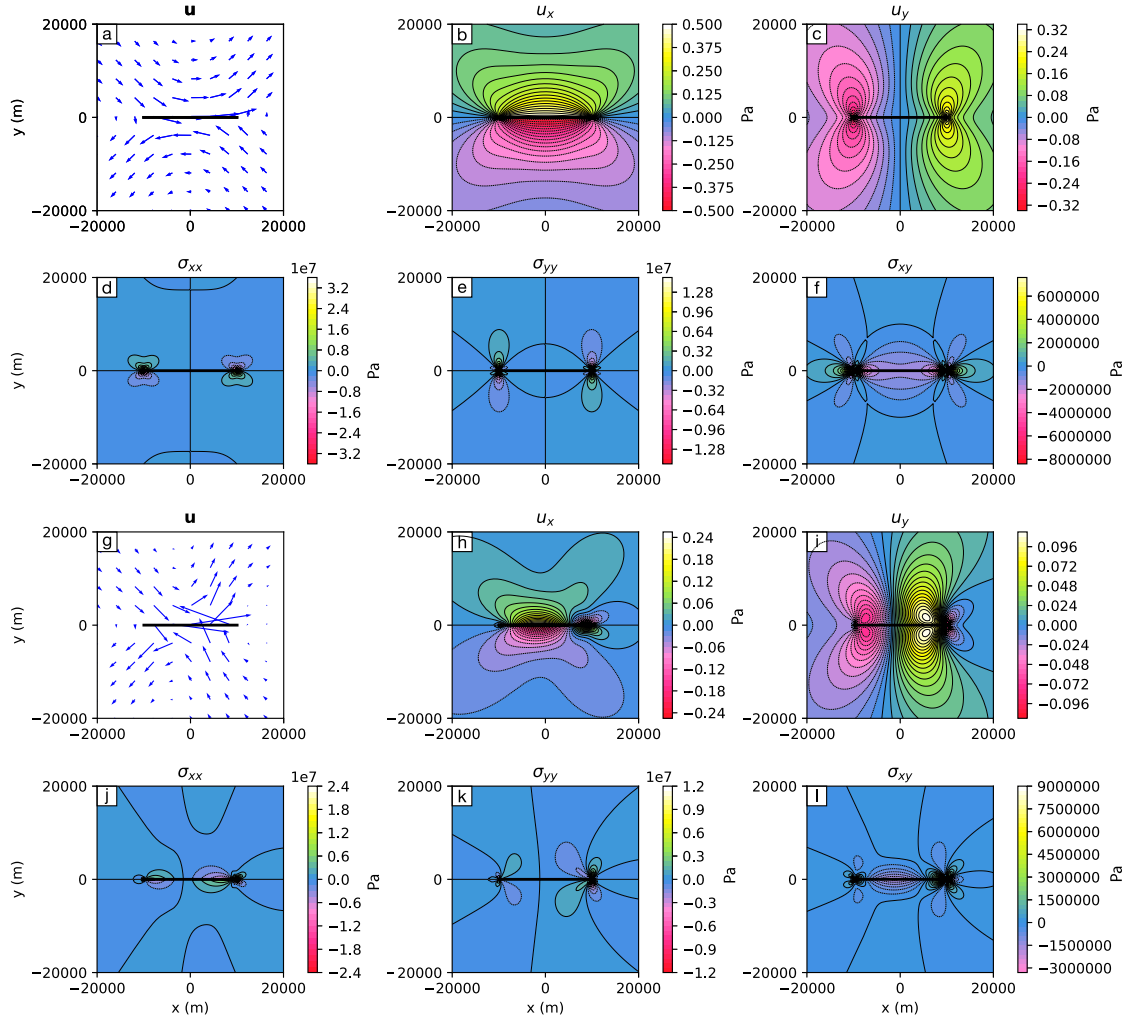
Fig. 1. Examples of the kernel displacements and stresses from full space plane strain CS (upper six panels) and 3QN (lower six panels) elements. Here we show near- and far-field displacements and stresses for a single planar element aligned along the x-axis with endpoints at $\pm10{,}000$ m. For the CS case we show the fields resulting from unit strike-slip and for the 3QN element a random quadratic distribution of strike-slip motion. For each of the six panel sequences the top left panel is the vector displacement field, the middle and right top row panels show contours of the x and y components of the displacement field and the bottom three panels show the σ_{xx}, σ_{yy} and σ_{xy} components of the stress tensor (from left to right).

2. The displacement discontinuity boundary element method for linear static elasticity

2.1. Overview

An array of distinct boundary element approaches for linear elasticity have been extensively developed and documented (e.g., Banerjee and Butterfield, 1981; Crouch and Starfield, 1983; Brebbia and Dominguez, 1994; Gaul et al., 2013). Here we follow the displacement discontinuity method (DDM) assuming the two-dimensional plane strain case for a non-inertial linear elastic body. The central idea behind the DDM is to represent the displacements and stresses throughout a model as the sum of displacement discontinuity Greens functions at the boundary of the domain. These Green's functions can represent the effects of displacement boundary conditions, traction boundary conditions, internal fault slip, and body forces,

$$\mathbf{u}(p) = \underbrace{\int_{C_{u+t}} \mathbf{T}^*(p, q_{C_{u+t}})\mathbf{u}^{\text{eff}}(q_{C_{u+t}})dC_{u+t}}_{\text{displacements from } u \text{ and } t \text{ boundaries}} + \underbrace{\int_{C_s} \mathbf{T}^*(p, q_{C_s})\mathbf{s}(q_{C_s})dC_s}_{\text{displacements from fault slip}}$$

$$+ \underbrace{\int_V \mathbf{K}_u^*(p, q_V)\mathbf{f}(q_V)dV}_{\text{displacements from body forces}} \quad (1)$$

$$\mathbf{s}(p) = \underbrace{\int_{C_{u+t}} \mathbf{S}^*(p, q_{C_{u+t}})\mathbf{u}^{\text{eff}}(q_{C_{u+t}})dC_{u+t}}_{\text{stresses from } u \text{ and } t \text{ boundaries}} + \underbrace{\int_{C_s} \mathbf{S}^*(p, q_{C_s})\mathbf{s}(q_{C_s})dC_s}_{\text{stresses from fault slip}}$$

$$+ \underbrace{\int_V \mathbf{K}_s^*(p, q_V)\mathbf{f}(q_V)dV}_{\text{stresses from body forces}} \quad (2)$$

Here $\mathbf{T}^*$, $\mathbf{K}_u^*$, $\mathbf{S}^*$, and $\mathbf{K}_s^*$ are kernel matrices (described in Section 2.2, Table 1) that relate displacements, fault slip, and body forces at source coordinates, q, to displacements and stresses at observation coordinates, p. The boundary surfaces with displacement, traction, and slip boundary conditions are denoted as C_u, C_t, and C_s, respectively with C_{u+t} indicating the combination of the displacement and traction boundaries. Body forces, $\mathbf{f}$, are applied within the interior volume, V, and may vary spatially. The displacements are given by $\mathbf{u}$. Also note that $\mathbf{s} = [\sigma_{xx}, \sigma_{yy}, \sigma_{xy}]$ is a vector that holds the flattened components of the stress tensor $\boldsymbol{\sigma}$. The "stress vector" can be used to calculated tractions on boundary with normal vector, $\mathbf{n}(p) = [n_x(p) \ n_y(p)]^{\text{T}}$, as $\mathbf{t} = \mathbf{N}\mathbf{s}$, where, $\mathbf{N} = \begin{bmatrix} n_x & n_y & 0 \\ 0 & n_x & n_y \end{bmatrix}$ so that the displacement to traction kernel is, $\mathbf{H}^* = \mathbf{N}\mathbf{S}^*$ and the body force to traction kernel is, $\mathbf{K}_t^* = \mathbf{N}\mathbf{K}_s^*$.

The central computational task associated with the DDM is to solve for $\mathbf{u}^{\text{eff}}$ given a distribution of displacement, $\mathbf{u}^{\text{bc}}$ and traction boundary
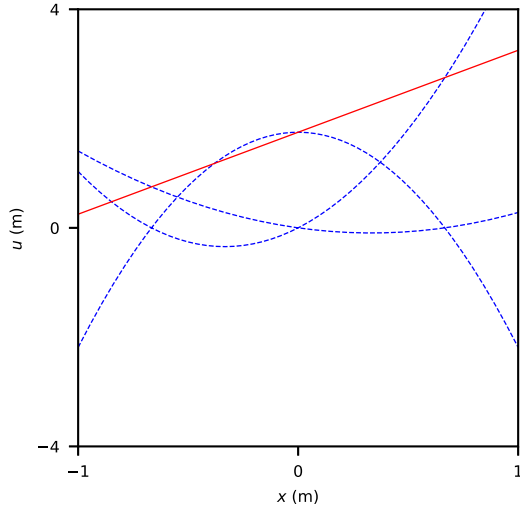
Fig. 2. Mode of construction of three quadratic node (3QN) elements. Here displacement discontinuity (slip) is specified not as a constant value over the element but as the sum of quadratic functions located at three distributed nodes. The spatial variation of slip along each element is then the sum of the three quadratics. This can reduce to constant or linear slip as well as represent quadratic slip.

Table 1

Overview of kernels and singularities as a function of distance, r, from observation point, p, from source location, q. The matrix shapes given in the left-most column are for a single constant slip element or the single point to point case.

| operation	Symbol	Source	Singularity	Shape
Displacement to displacement	$\mathbf{T}^*$	Line	r^{-1}	2×2
Displacement to traction	$\mathbf{H}^* = \mathbf{N}\mathbf{S}^*$	Line	r^{-2}	2×2
Displacement to stress	$\mathbf{S}^*$	Line	r^{-2}	3×2
Force to displacement	$\mathbf{K}_u^*$	Point	r^{-1}	2×2
Force to traction	$\mathbf{K}_t^* = \mathbf{N}\mathbf{K}_s^*$	Point	r^{-2}	2×2
Force to stress	$\mathbf{K}_s^*$	Point	r^{-2}	3×2

the traction version of Eq. (2),

$$\begin{bmatrix} \mathbf{u}^{\text{bc}}(p_{C_u}) \\ \mathbf{t}^{\text{bc}}(p_{C_t}) \end{bmatrix} = \begin{bmatrix} \bar{\mathbf{T}}^*(p_{C_u}, q_{C_{u+t}}) \\ \bar{\mathbf{H}}^*(p_{C_t}, q_{C_{u+t}}) \end{bmatrix} \mathbf{u}^{\text{eff}}(q_{C_{u+t}}) + \begin{bmatrix} \bar{\mathbf{T}}^*(p_{C_u}, q_{C_s}) & \bar{\mathbf{K}}_u^*(p_{C_u}, q_V) \\ \bar{\mathbf{H}}^*(p_{C_t}, q_{C_s}) & \bar{\mathbf{K}}_t^*(p_{C_t}, q_V) \end{bmatrix}$$
$$\times \begin{bmatrix} \mathbf{s}^{\text{bc}}(q_{C_s}) \\ \mathbf{f}(q_V) \end{bmatrix} \tag{3}$$

and then solve for $\mathbf{u}^{\text{eff}}(q_C)$,

$$\mathbf{u}^{\text{eff}}(q_{C_{u+t}}) = \begin{bmatrix} \bar{\mathbf{T}}^*(p_{C_u}, q_{C_{u+t}}) \\ \bar{\mathbf{H}}^*(p_{C_t}, q_{C_{u+t}}) \end{bmatrix}^{-1} \left\{ \begin{bmatrix} \mathbf{u}^{\text{bc}}(p_{C_u}) \\ \mathbf{t}^{\text{bc}}(p_{C_t}) \end{bmatrix} \right.$$
$$\left. - \begin{bmatrix} \bar{\mathbf{T}}^*(p_{C_u}, q_{C_s}) & \bar{\mathbf{K}}_u^*(p_{C_u}, q_V) \\ \bar{\mathbf{H}}^*(p_{C_t}, q_{C_s}) & \bar{\mathbf{K}}_t^*(p_{C_t}, q_V) \end{bmatrix} \begin{bmatrix} \mathbf{s}^{\text{bc}}(q_{C_s}) \\ \mathbf{f}(q_V) \end{bmatrix} \right\}. \tag{4}$$

conditions $\mathbf{t}^{\text{bc}}$, internal displacement discontinuities, $\mathbf{s}^{\text{bc}}$, and set of body forces, $\mathbf{f}$. To do this we simultaneously evaluate equation (1) and

All of the integrals in Eqs. (1), (2) have been replaced with their matrix equivalents (denoted with an overbar, " ‾ ") in Eqs. (3), (4).
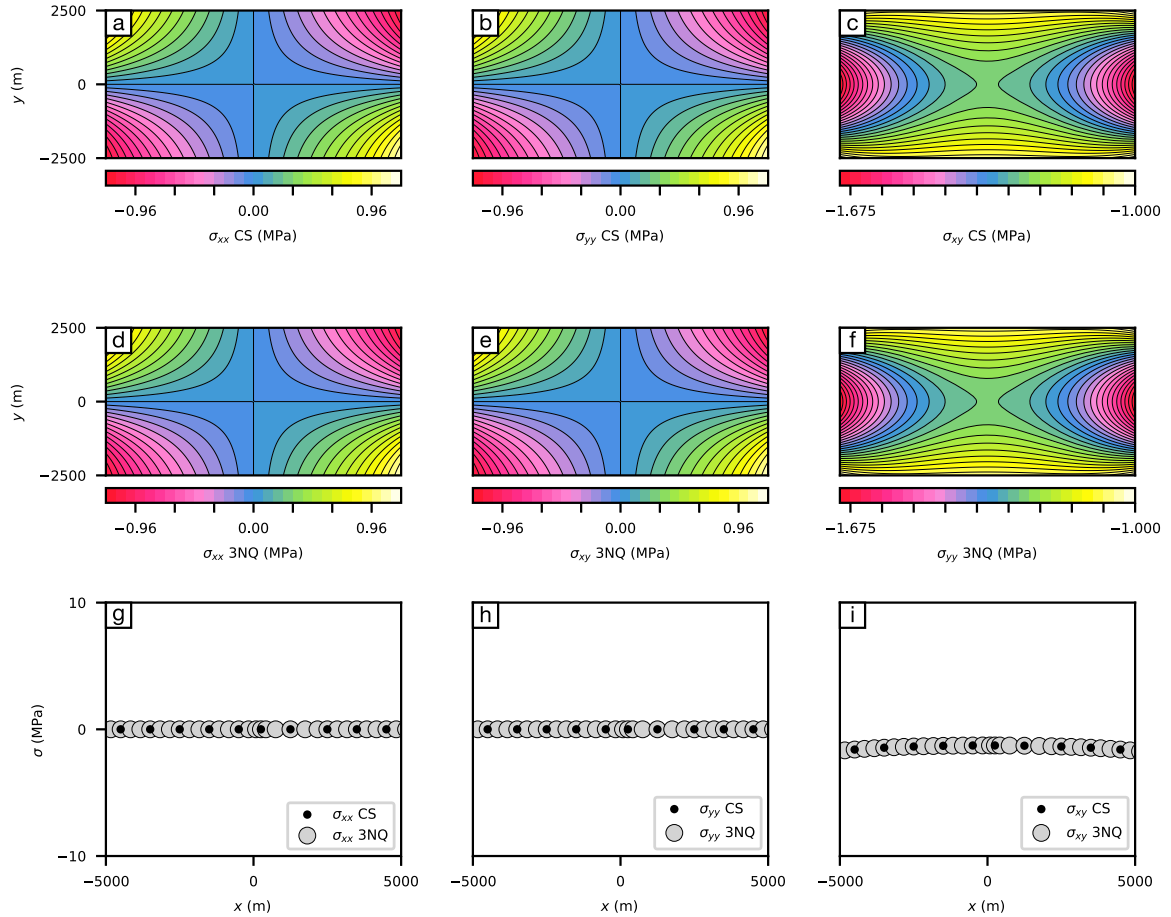
Fig. 3. Coincident, near-, and far-field stresses for the forward evaluation of elements approximating constant slip along a planar fault surface discretized into sub elements. Near- and far-field stresses for the constant element and 3QN elements are shown in the upper and middle rows respectively. The bottom row shows the coincident stresses on element nodes for both cases. Slip along each element is identical and the gradient is associated with the finite extent of the boundary elements which extend outside of the plotted domain. Here the two cases are identical and this figure serves as a baseline for comparison with Fig. 4.
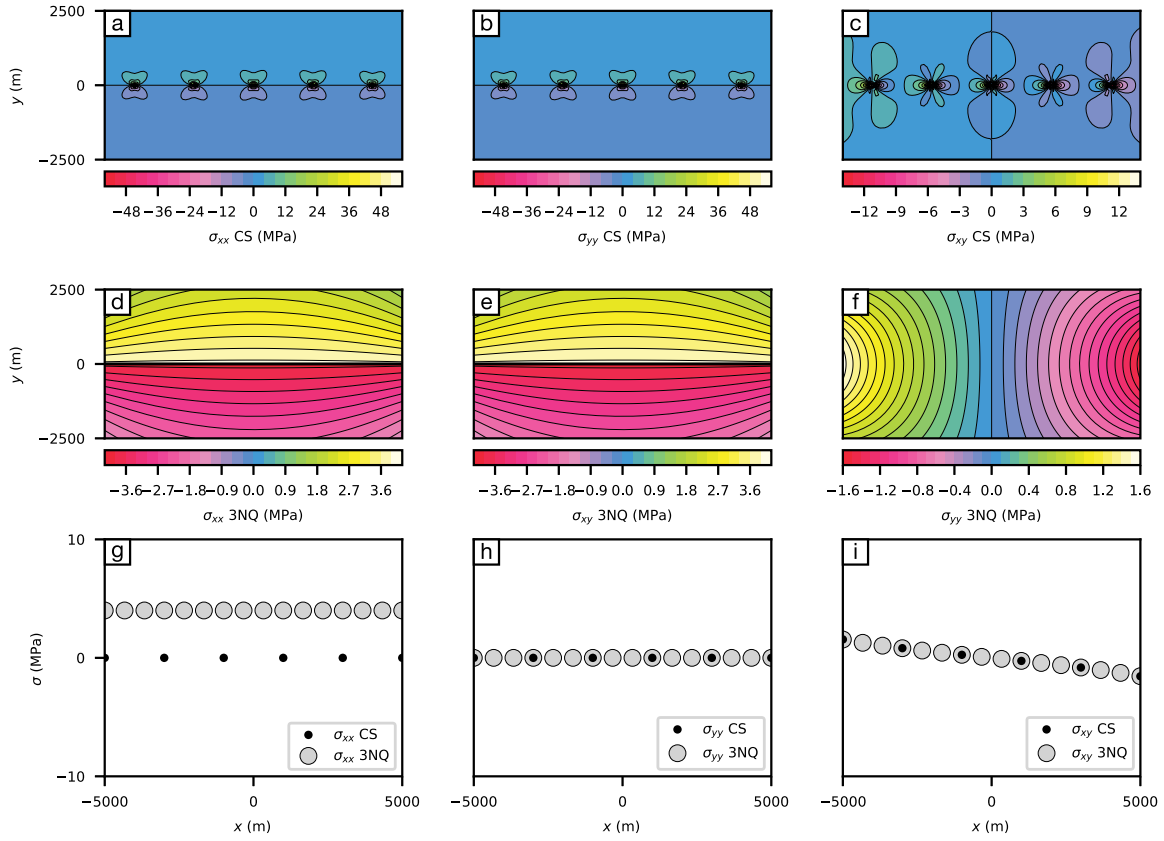
Fig. 4. Coincident, near-, and far-field stresses for the forward evaluation of a constant slip elements approximating a linear gradient in slip along a planar fault surface discretized into sub elements. Near- and far-field stresses for the constant element and 3QN elements are shown in the upper and middle rows respectively. The bottom row shows the coincident stresses on element nodes for both cases. For the constant slip case the slip gradient is approximated as constant slip over each element. For the 3QN case a linear slip gradient can be represented exactly by constructing linear slip profiles for each element. Two notable differences between the two cases. The first is that near-field stresses for the constant slip element case exhibit strong gradients at element edges due do the discontinuity in slip which are not present in the linear-3QN case. The difference between the first and second rows demonstrate this effect. The second difference is seen by inspection of the coincident nodal stresses (bottom row). The most notable effect is that σ_{xx} stresses are remarkably different for the two cases. For the CS element case the are exactly zero because each element has no slip gradient on itself. In contrast the coincident σ_{xx} stresses for the 3QN case are constant and non-zero reflecting the constant slip gradient across both each element and the collective set of elements.

While this may seem a cogent approach it is numerically challenging to calculate $\bar{\mathbf{K}}_t^*$ due to the strongly singular nature of the $\mathbf{K}_t^*$ kernel. Because the integration of Kelvin kernels over arbitrary domains is difficult several approaches have been developed for the simplified case of a body force that is the same everywhere (e.g., Rizzo and Shippy, 1977). Here we follow the particular integral method (Pape and Banerjee, 1987) and replace the body force integral with a set of gravitationally generated displacements and stresses that modulate the effective displacement and traction boundary conditions to reproduce the effect of unidirectional gravity,

$$
\mathbf{u}^{\text{eff}}(q_{C_{u+t}}) = \begin{bmatrix} \bar{\mathbf{T}}^*(p_{C_u}, q_{C_{u+t}}) \\ \bar{\mathbf{H}}^*(p_{C_t}, q_{C_{u+t}}) \end{bmatrix}^{-1} \left\{ \begin{bmatrix} \mathbf{u}^{\text{bc}}(p_{C_u}) - \mathbf{u}_{\text{g}}^{\text{bc}}(p_{C_u}) \\ (\mathbf{t}^{\text{bc}}(p_{C_t}) - \mathbf{t}_{\text{g}}^{\text{bc}}(p_{C_t})) \end{bmatrix} \right.
$$
$$
\left. - \begin{bmatrix} \bar{\mathbf{T}}^*(p_{C_u}, q_{C_s}) \\ \bar{\mathbf{H}}^*(p_{C_t}, q_{C_s}) \end{bmatrix} \mathbf{s}^{\text{bc}}(q_{C_s}) \right\}. \tag{5}
$$

At a single boundary node the displacements and tractions that modify the true displacement and traction boundary conditions are given by, $\mathbf{u}_{\text{g}}^{\text{bc}} = [-\lambda \rho g x y /(4\mu(\lambda+\mu)) \quad \rho g(\lambda x^2 + (\lambda+2\mu)y^2)/(8\mu(\lambda+\mu))]^{\text{T}}$ and $\mathbf{t}_{\text{g}}^{\text{bc}} = [0 \quad \rho g y n_y]^{\text{T}}$ (Pape and Banerjee, 1987). After solving for $\mathbf{u}_{\text{eff}}$, the displacements and stresses everywhere in the interior of the volume can be calculated noting the caveats below. Note that the matrix solution may require preconditioning to avoid large conditions numbers.

2.2. Constant three node quadratic kernels for finite length elements

Crouch and Starfield (1983) summarize the $\mathbf{T}^*$ and $\mathbf{S}^*$ kernels (from which $\mathbf{H}^*$ can be calculated) for a single constant slip (CS) boundary element in an unbounded and homogeneous medium with an element aligned along the x axis and ranging form $-a$ to a. These kernels can be factored into a form that isolates the x dependence of the solution into a set of functions f_i,

$$
\mathbf{T}^* = \mathbf{R}\mathbf{T} = \mathbf{R} \begin{bmatrix} 2(1-\nu)f_2 - yf_5 & (1-2\nu)f_3 - yf_4 \\ (1-2\nu)f_3 - yf_4 & 2(1-\nu)f_2 + yf_5 \end{bmatrix} \tag{6}
$$

$$
\mathbf{S}^* = \mathbf{R}\mathbf{S} = 2\mu\mathbf{R} \begin{bmatrix} 2f_4 + yf_6 & -f_5 + yf_7 \\ -yf_6 & -f_5 - yf_7 \\ -f_5 + yf_7 & -yf_6 \end{bmatrix} \tag{7}
$$

Here ν is Poisson's ratio and μ is the shear modulus. The functions $f_i(x, y, a)$ depend only on element geometry observation coordinates (x, y) and the element half-length (Appendix).

A higher order representation of element slip is possible using three node quadratic (3QN) elements (e.g., Portela et al., 1992). The central idea is to replace constant displacement discontinuity elements with quadratic displacement discontinuity elements. The particular formulation of 3QN enables the construction of constant, linear, and quadratic slip profiles by the superposition of three quadratic shape functions located at equally spaced nodes along each boundary element (2). Three node quadratic elements can be obtained by replacing the constant slip functions $f_i(x, y, a)$ in Eqs. (16)–(22) with a new set of functions $g_{i,j}(x, y, a)$. Here $i = 1 - 7$ as in f_i and $k = 1 - 3$ for each of three quadratic shape functions, one for each node, $\phi_1 = c_1 x(9x/8a - 3/4)/a$, $\phi_2 = c_2(1 - 3x/2a)(1 + 3x/2a)$, $\phi_3 = c_3 x(9x/8a + 3/4)/a$. We can relate the shape functions and the CS element function, f_i to $g_{i,j}$ as,

$$
g_{i,j}(x, y, a) = \int_{-a}^{a} \phi_j(x, a) \frac{df_i(x, y, a)}{da} da. \tag{8}
$$
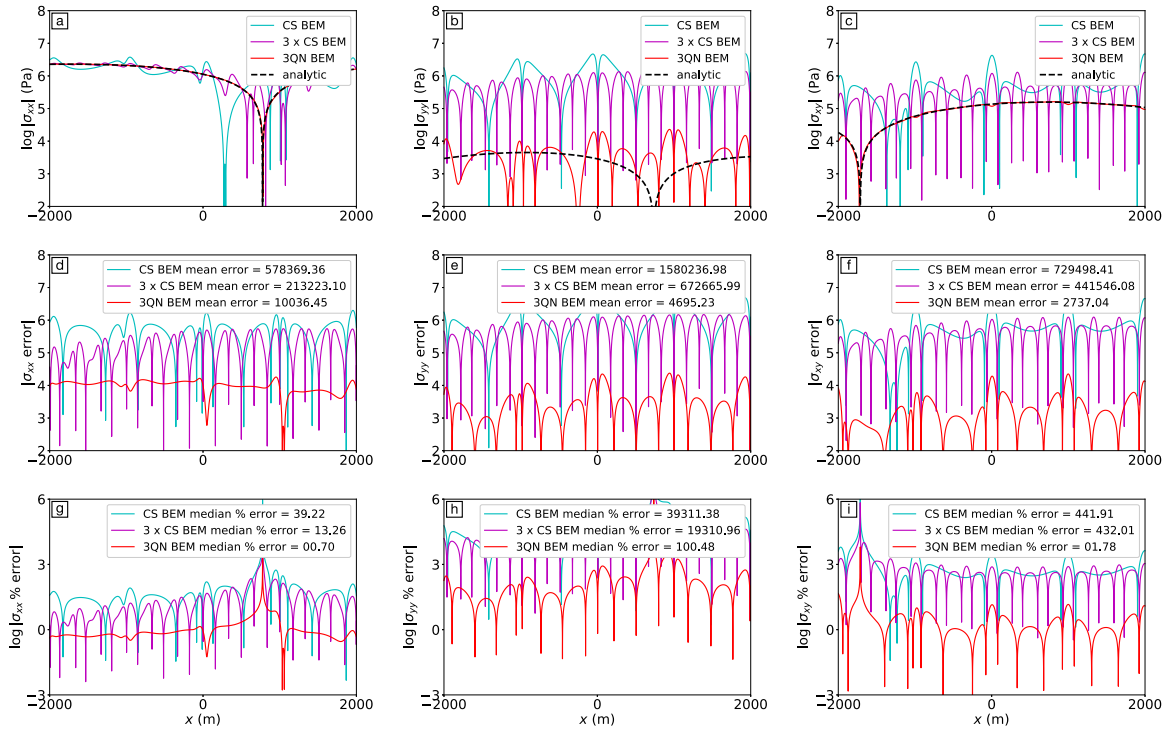
Fig. 5. A comparison of near-field errors from discontinuous CS and discontinuous 3QN element BEMs. The model geometry is a free surface extending ±100 km from $x = 0$ with 10 km wide fault dipping at 45 degrees buried 10 km below the free surface. The fault has 1 m of dip slip motion. Near-field stresses (evaluated 100 m below the free surface) calculated from four models: (1) An analytic halfspace solution (dashed black line) (Okada, 1992), (2) a CS BEM with 200 elements (solid (?)cyan line), (3) a CS BEM with 600 elements (solid light purple line), and (4) a 3QN BEM BEM with 200 elements (600 nodes, solid red line). The upper row shows the three stress components, the middle row shows the absolute error and the lower row shows the percentage error. Both the CS and 3QN element cases exhibit the largest residuals near element boundaries as a result of element to element slip discontinuities. In general, CS BEM residuals are larger than 3QN based model even for the same number of nodes (600 element CS BEM vs. 200 element 3QN BEM). (For interpretation of the references to color in this figure legend, the reader is referred to the web version of this article.)

This is sufficient for the far-field evaluation. However, the coincident ($p = q$) case must be evaluated at the element nodes and we again need a new set of functions to replace f_i. These are $h_{i,j}(a) = \lim_{y \to 0} g_{i,j}(x, y, a)$. We computed integrals symbolically with the maxima symbolic mathematics tool (http://maxima.sourceforge.net/). The closed form analytic forms are not presented in this document because they are very long but are coded at: https://github.com/brendanjmeade/Bem2d.jl/src/Bem2d.jl.

An additional and necessary step is to relate the shape function coefficients c_i to the displacement discontinuity/fault slip Δu_i at each node. We can do this by solving for the coefficients c_i that multiply each shape function ϕ_i to give the variation in slip. All we need to do is solve the linear system with slip sampled at the locations of the three element nodes, $u(x_1), u(x_2), u(x_3)$,

$$\begin{bmatrix} c_1 \\ c_2 \\ c_3 \end{bmatrix} = \begin{bmatrix} \phi_1(x_1, a) & \phi_2(x_1, a) & \phi_3(x_1, a) \\ \phi_1(x_2, a) & \phi_2(x_2, a) & \phi_3(x_2, a) \\ \phi_1(x_3, a) & \phi_2(x_3, a) & \phi_3(x_3, a) \end{bmatrix}^{-1} \begin{bmatrix} \Delta u(x_1) \\ \Delta u(x_2) \\ \Delta u(x_3) \end{bmatrix},$$

(9)

Finally we can construct the linear operators that take the displacement discontinuities at the three nodes of a quadratic element and predict the displacements and tractions at observation points,

$$\mathbf{T}^*_{\text{quad}} = \begin{bmatrix} \mathbf{RT}(g_{2-5,1}(u_1, x, y, a)) & \mathbf{RT}(g_{2-5,2}(u_2, x, y, a)) & \mathbf{RT}(g_{2-5,3}(u_3, x, y, a)) \end{bmatrix}$$

(10)

$$\mathbf{S}^*_{\text{quad}} = \begin{bmatrix} \mathbf{RS}(g_{4-7,1}(u_1, x, y, a)) & \mathbf{RS}(g_{4-7,2}(u_2, x, y, a)) & \mathbf{RS}(g_{4-7,3}(u_3, x, y, a)) \end{bmatrix}.$$

(11)

In practice, these are the quadratic element replacements for Eqs. (6), (7). Coincident cases can be handled similarly with the replacement of $h_{i,j}$ for $g_{i,j}$.

2.3. A comparison of constant and quadratic elements

The reason that we have described 3QN elements is that they provide some properties that are distinct from CS elements. Specifically, constant slip elements face challenges with respect to their accuracy in the presence of slip gradients. Slip gradients are often approximated by discretizing and boundary into a finite number of elements and then representing the overall slip gradient with an evaluation of the slip gradient function at element nodes. This approximation is accurate in the far-field and known to be inaccurate near-field (within 1 element length) because displacement between adjacent CS elements is discontinuous. Further, the coincident determination of the full stress tensor at CS element nodes is also incomplete. Three quadratic node elements allow for the recovery of the full stress tensor at element nodes and increased accuracy for near-field evaluations (see Fig. 1).

To illustrate this behavior we consider a geometrically simple example consisting of an array of 20 planar elements aligned along the x-axis from $-10\,000$ to $10\,000$ m. For the case of uniform (constant) fault parallel (x-direction only) slip across all elements both CS and 3QN elements give the exact same answer (Fig. 3) however, for the case of a simple linear slip gradient across the two solutions differ (Fig. 4). The reason for this is that for the 3QN elements (which can be used to create a linear slip element) the slip distribution is everywhere continuous (with the exception of the endpoints of the array of elements) and that the 3QN elements. This difference can be seen most clearly when looking at the elements of the stress tensor evaluated on element nodes. The largest difference between the CS and 3QN elements is for the σ_{xx} stress component. For the geometry and applied slip of this particular case these are exactly zero. The reasons for this are (1) slip is assumed to constant over each CS element so individual element has information about the slip gradient (i.e., zero self-interaction) and (2) all of elements are arrayed along a line that is
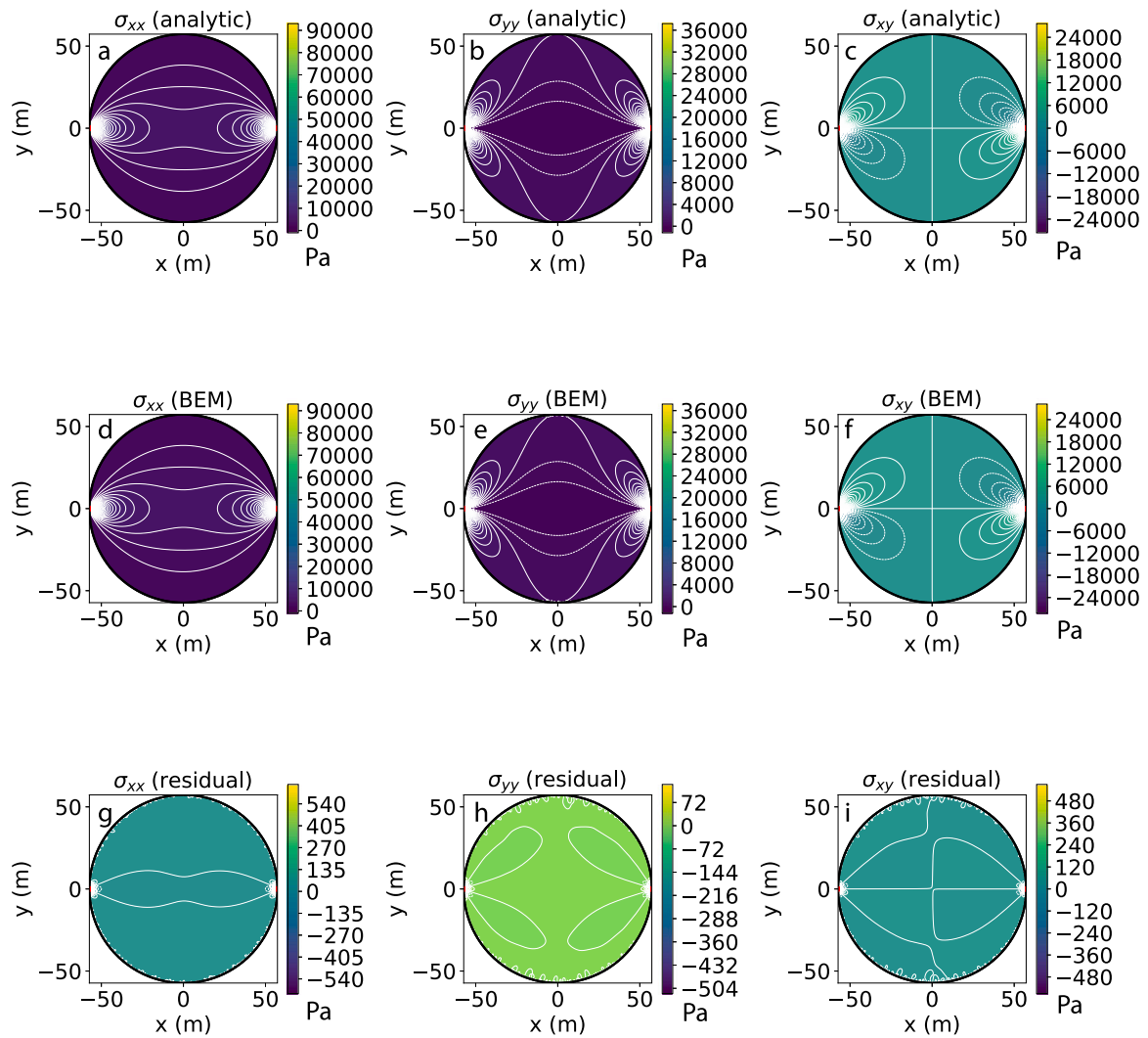
Fig. 6. Analytic and quadratic BEM comparison for with the analytic solution for the Brazil test uniform compression of a homogeneous disc, Hondros (1959). The σ_{xx}, σ_{yy}, σ_{xy} stress components are shown in the left, center, and right columns respectively. The analytic solutions, quadratic BEM, and residuals are shown in the top, middle, and bottom rows respectively.

coincident with the nodal plane for constant slip elements at $y = 0$. . Because 3QN elements can represent linear slip exactly on each element the σ_{xx} stresses are accurate for both the centroids and the two other nodal coordinates for these elements.

While this naive implementation of 3QN elements does allow for the accurate calculation of the full stress tensor at element nodes and in the far-field (as do CS elements) near field inaccuracies are still present because in general we do not assume that slip is continuous from element to element. This means that 3QN elements still exhibit unphysical singularities at element boundaries. To highlight this effect and show the impact the continued use of discontinuous element to element slip we compare the exact solution for a thrust fault in a half space (Okada, 1985, 1992) with a BEM approximation. Having an analytic solution for this case allows us to assess the near-field error associated with both constant slip and 3QN elements. To do this we construct a simple example of a thrust fault inclined at 45° intersecting with a flat free surface constructed of uniformly sized boundary elements. We evaluate the accuracy of the two BEM elements by considering the stresses immediately below but not on the free surface. The distance below the free surface was chosen to be equal to that between any two nodes in 3QN element. As expected the BEM errors peak near element boundaries for both constant and 3QN elements (Fig. 5). However for this simple case the mean absolute error

may be 10+ times larger for the constant case when compared with the 3QN case. These two idealized cases show how 3QN elements can be used to accurately model on fault stress at nodal coordinates but still require care when considering near field off-fault evaluations.

3. DDM solutions to reference problems

3.1. A compressed disc

The Brazil test (Hondros, 1959) is a reference problem that involves the displacements and stresses interior to a circular disc in response to tractions applied along the disc perimeter. In this case there are only applied traction boundary conditions, $C_u = \emptyset$, no internal displacement discontinuities, $C_s = \emptyset$, nor body forces $\mathbf{f}(q_V) = \emptyset$. This reduces equation (4) to $\mathbf{t}^{bc}(p_{C_t}) = \bar{\mathbf{H}}^*(p_{C_t}, q_C)\mathbf{u}^{eff}(q_C)$, and we can solve for the effective boundary displacements with,

$$\mathbf{u}^{eff}(q_C) = \bar{\mathbf{H}}^{*-1}(p_{C_t}, q_C)\mathbf{t}^{bc}(p_{C_t}). \tag{12}$$

From this we can obtain the effective displacements induced by the applied tractions and the internal stresses (Fig. 6). Note that the BEM solution is compared with an analytic solution that is expressed as a series solution so that the transition from non-zero to zero tractions
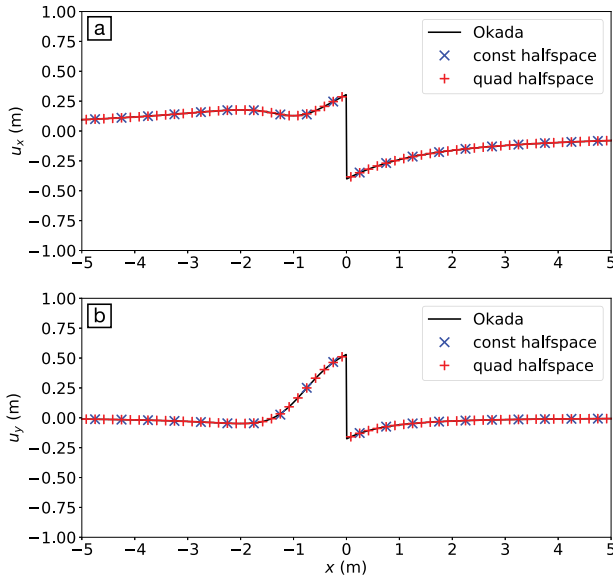
Fig. 7. Surface displacements from analytic half space solution solutions and boundary element approximations. The BEM free surface extends ±50 m to either side of the fault trace. The fault dips at 45° with a down-dip width of $\sqrt{2}/2$ m. The solid black line is the analytic solution the blue x's are the constant slip BEM solution and the red crosses are the quadratic BEM solutions. x- and y-displacements are shown in the upper and lower panels respectively.
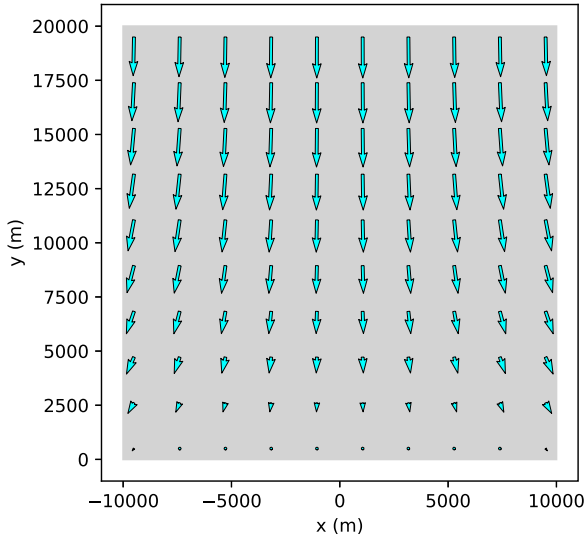

Fig. 8. Total displacements for a square under gravitational load example. Max vertical displacement is 65 m. Max horizontal displacement is 12 m.

is as the exact problem description. As written, because this solution admits an arbitrary rigid-body translation, the resulting linear system is poorly conditioned. This can be improved with either displacement constraints and/or matrix preconditioning.

3.2. A fault and a free surface

A classic problem in earthquake cycle modeling is the determination of surface displacements due to slip on a fault at depth in a homogeneous elastic half space (Okada, 1985, 1992). We consider the case of constant slip on a single thrust fault intersecting with the free surface and inclined at 45°. For this case there are no body forces and the free surface is approximated as a traction free boundary. Physically we can think of the free surface displacements as those that will be generated

by a set of tractions that cancel out the tractions induced by the fault in a full space. In this case the expression for $\mathbf{u}^{\text{eff}}(q_{\text{surface}})$ (Eq. (4)) reduces to,

$$\mathbf{u}^{\text{eff}}(q_{\text{surface}}) = \bar{\mathbf{H}}^{*-1}(p_{\text{surface}}, q_{\text{surface}})\bar{\mathbf{H}}^*(p_{\text{surface}}, q_{\text{fault}})\mathbf{s}^{\text{bc}}(q_{\text{fault}}). \quad (13)$$

Here $\mathbf{u}^{\text{eff}}(q_C)$ actually gives the free surface displacements at the boundary element nodes where it is evaluated (Fig. 7). Note that while the example here is for a flat halfspace the formulas are exactly the same for the case where the free surface is non-planar.

3.3. An elastic block under gravitational load

We now consider a case with no analytic solution to compare with but of interest nonetheless because it allows for demonstration of how DDM solutions with gravity can be assembled. We model a square domain with its center at the origin and extending ±10 km in the x and y directions with no interior displacement discontinuities. The entire block is subject to the force of gravity acting in the $-y$ direction with a no slip basal boundary condition on the B(ottom) edge, $\mathbf{u}^{\text{bc}}(p_{C_B}) = 0$, and traction free boundary conditions along the R(ight), T(op), and L(eft) edges, $\mathbf{t}^{\text{bc}}(p_{C_{R+T+L}}) = 0$. For the vertical side walls of the model, $n_y = 0$ and so the gravitational particular solutions vanish on the left and right hand sides of the square. This reduces equation (5) to,

$$\mathbf{u}^{\text{eff}}(q_{C_{B+R+T+L}}) = - \begin{bmatrix} \bar{\mathbf{T}}^*(p_{C_B}, q_{C_{B+R+T+L}}) \\ \bar{\mathbf{H}}^*(p_{C_{R+T+L}}, q_{C_{B+R+T+L}}) \end{bmatrix}^{-1} \begin{bmatrix} \mathbf{u}^{\text{bc}}_g(p_{C_B}) \\ 0(p_{C_R}) \\ \mathbf{t}^{\text{bc}}_g(p_{C_T}) \\ 0(p_{C_L}) \end{bmatrix} \quad (14)$$

The calculation reveals that the gravitational collapse decreases the total elevation of the initially square block with maximum horizontal displacements 12 m approximately 1/3rd of the way up from the bottom boundary (Fig. 8).

### 3.4. A finite body with topographic relief and fault under gravitational load

We lastly illustrate a model with an embedded fault with known slip under gravitational load below topography and compare this to the case where there is no topographic gradient. We model a square domain with its center at the origin and extending ±10 km in the x and y directions with no interior displacement discontinuities. The entire block is subject to the force of gravity acting in the $-y$ direction with a no slip basal boundary condition on the B(ottom) edge, $\mathbf{u}^{\text{bc}}(p_{C_B}) = 0$, and traction free boundary conditions along the R(ight), T(op), and L(eft) edges, $\mathbf{t}^{\text{bc}}(p_{C_{R+T+L}}) = 0$. For the vertical side walls of the model, $n_y = 0$ and so the gravitational particular solutions vanish on the left and right hand sides of the square. This reduces equation (5) to,

$$\begin{aligned} \mathbf{u}^{\text{eff}}(q_{C_{B+R+T+L}}) &= \begin{bmatrix} \bar{\mathbf{T}}^*(p_{C_B}, q_{C_{B+R+T+L}}) \\ \bar{\mathbf{H}}^*(p_{C_{R+T+L}}, q_{C_{B+R+T+L}}) \end{bmatrix}^{-1} \\ &\times \left\{ \begin{bmatrix} \mathbf{u}^{\text{bc}}(p_{C_B}) - \mathbf{u}^{\text{bc}}_g(p_{C_B}) \\ (\mathbf{t}^{\text{bc}}(p_{C_{R+T+L}}) - \mathbf{t}^{\text{bc}}_g(p_{C_{R+T+L}})) \end{bmatrix} - \begin{bmatrix} \bar{\mathbf{T}}^*(p_{C_B}, q_{C_s}) \\ \bar{\mathbf{H}}^*(p_{C_{R+T+L}}, q_{C_s}) \end{bmatrix} \mathbf{s}^{\text{bc}}(q_{C_s}) \right\}. \end{aligned} \quad (15)$$

Results for the flat and non-flat cases are shown in Figs. 9 and 10. Note that the combination of both faulting and gravity with this particular formulation is not particularly useful for the problem of evaluating coseismic slip including gravitational body forces. The reason for this is that for quasi-static/dynamic problems the influence of gravity enters into the problem as a result of a change in the shape of the domain. In other words the gravitational contribution to coseismic deformation would require an evaluation of difference in gravitational deformation between the pre- and post-earthquake boundary geometries and this would require advecting the boundary mesh with the non-gravitational coseismic displacements. The greater utility of the combined gravitational and faulting approach is for evaluating the stress state and mechanical stability of fault system and topographic configurations over tectonic time scales.
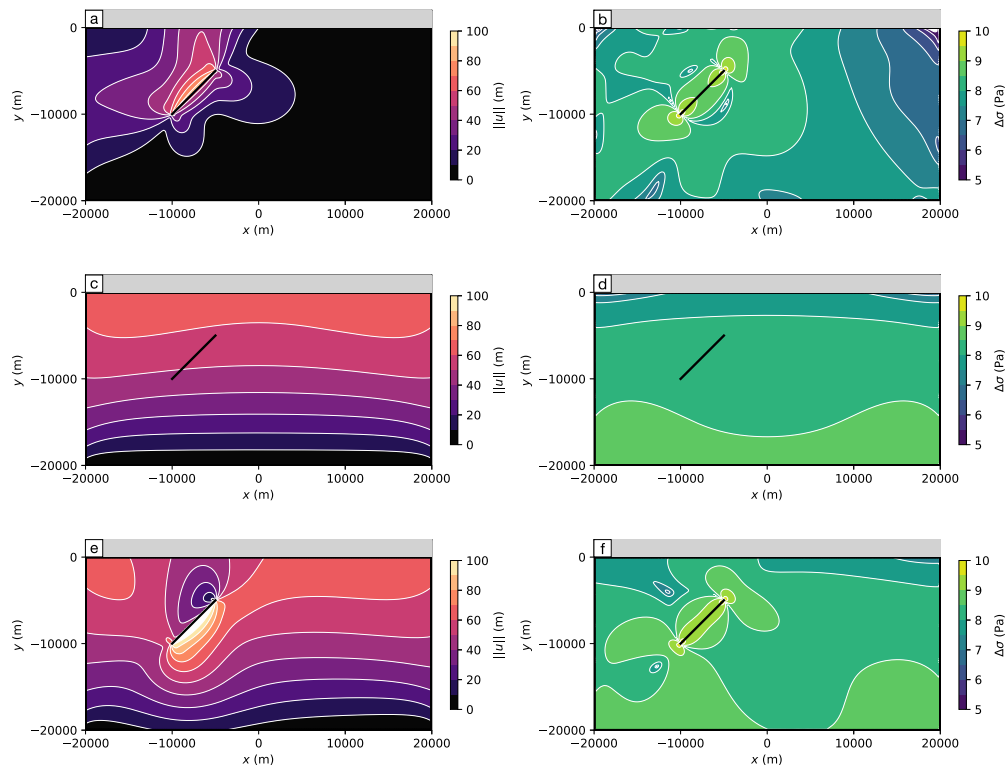
Fig. 9. Displacement magnitudes and difference in principle stresses for fault in a finite domain with no gravity (top row), gravity only (middle row), and fault slip with gravity. Boundary conditions are zero slip at the base and traction free on the right, top, and left sides. Note that the 100 m magnitude of fault slip here is intentionally chosen to be larger than typical coseismic slip so that the combined gravity and faulting solution is not dominated by the gravitational signal alone. For this sort of tectonic problem the gravitational collapse is nearly 100 m and when combined with fault slip may significantly modify the lateral decay in differential stress and may reduce the faulting contribution to topographic growth.
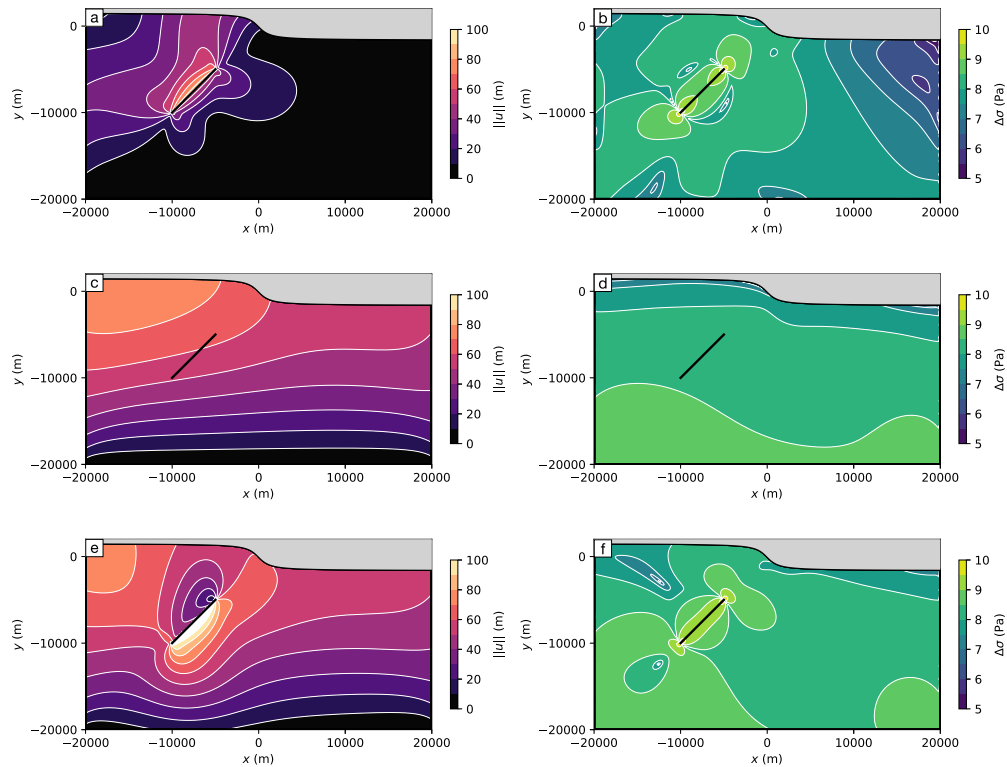
Fig. 10. Same as Fig. 9 with ~ 2 km of topographic relief. The excess topography above the fault reduces the magnitude of surface deformation and introduces short wavelength variations in differential stress magnitudes in the vicinity of the greatest topographic slope.

4. Conclusions

Boundary elements models have been and continue to be commonly used methods for developing and understanding mechanical models of earthquake cycle and tectonic behavior due to the flexibility of their boundary model representation. Here we described code that combines and implements two classical boundary element ideas: (1) higher order element shape functions and (2) gravity. With these two approaches it is possible to accurately solve and evaluate linear elastic problems at element nodes including the complete stress tensor and the effects of gravity. In particular we use quadratic boundary elements and provide closed form solution for both the far-field and coincident cases. We find that near-field errors in the evaluation of the stress tensor are smaller with quadratic boundary elements when compared with constant slip boundary elements. However, while smaller, the near-field errors may still be significant enough to render this BEM approach inaccurate for problems focusing on off-fault plastic yielding. Further we show that the particular solution approach to gravity can be integrated with internal faulting and non-planar topography problems to accurately assess the state of tectonics stress away from model boundaries.

Declaration of competing interest

The authors declare that they have no known competing financial interests or personal relationships that could have appeared to influence the work reported in this paper.

Code availability:

https://github.com/brendanjmeade/Bem2d.jl.

Acknowledgments

Appendix. Constant displacement element kernel functions

Crouch and Starfield (1983) concisely summarized the closed form expressions for the displacements and stresses due to a finite width displacement discontinuity in a homogeneous elastic halfspace under plane strain conditions. These expressions are,

$$f_1 = y\tan^{-1}\frac{y}{x+a} - y\tan^{-1}\frac{y}{x-a} + (x-a)\log\sqrt{(x-a)^2+y^2}$$
$$- (x+a)\log\sqrt{(x+a)^2+y^2} \tag{16}$$

$$f_2 = \frac{df_1}{dy} = \tan^{-1}\frac{y}{x+a} - \tan^{-1}\frac{y}{x-a} \tag{17}$$

$$f_3 = \frac{df_1}{dx} = \log\sqrt{(x-a)^2+y^2} - \log\sqrt{(x+a)^2+y^2} \tag{18}$$

$$f_4 = \frac{df_1}{dxy} = \frac{y}{(x-a)^2+y^2} - \frac{y}{(x+a)^2+y^2} \tag{19}$$

$$f_5 = \frac{df_1^2}{dx^2} = \frac{x-a}{(x-a)^2+y^2} - \frac{x+a}{(x+a)^2+y^2} \tag{20}$$

$$f_6 = \frac{df_1^3}{dxy^2} = \frac{(x-a)^2-y^2}{((x-a)^2+y^2)^2} - \frac{(x+a)^2-y^2}{((x+a)^2+y^2)^2} \tag{21}$$

$$f_7 = \frac{df_1^3}{dx^2y} = \frac{x-a}{((x-a)^2+y^2)^2} - \frac{x+a}{((x+a)^2+y^2)^2} \tag{22}$$

and they can be used to construct $\mathbf{T}^*$ and $\mathbf{S}^*$.

References

Banerjee, P.K., Butterfield, R., 1981. Boundary Element Methods in Engineering Science, Vol. 17. McGraw-Hill London.

Bendick, R., Bilham, R., Freymueller, J., Larson, K., Yin, G.H., 2000. Geodetic evidence for a low slip rate in the Altyn Tagh fault system. Nature 404 (6773), 69–72.

Bilham, R., Larson, K., Freymueller, J., Jouanne, F., LeFort, P., Leturmy, P., Mugnier, J.L., Gamond, J.F., Glot, J.P., Martinod, J., Chaudury, N.L., Chitrakar, G.R., Gautam, U.P., Koirala, B.P., Pandey, M.R., Ranabhat, R., Sapkota, S.N., Shrestha, P.L., Thakuri, M.C., Timilsina, U.R., Tiwari, D.R., Vidal, G., Vigny, C., Galy, A., deVoogd, B., 1997. GPS measurements of present-day convergence across the Nepal Himalaya. Nature 386 (6620), 61–64.

Brebbia, C.A., Dominguez, J., 1994. Boundary Elements: An Introductory Course. WIT Press.

Brown, R.L., 1975. A Dislocation Approach to Plate Interaction (Ph.D. thesis). Massachusetts Institute of Technology.

Burgmann, R., Ergintav, S., Segall, P., Hearn, E.H., McClusky, S., Reilinger, R.E., Woith, H., Zschau, J., 2002. Time-dependent distributed afterslip on and deep below the Izmit earthquake rupture. Bull. Seismol. Soc. Am. 92 (1), 126–137.

Comninou, M., 1973. Angular Dislocation in a Half Space (Ph.D. thesis). Northwestern University, Chicago, IL.

Crouch, S.L., Starfield, A.M., 1983. Boundary Element Methods in Solid Mechanics. Allen and Unwin, London.

Dieterich, J.H., 1992. Earthquake nucleation on faults with rate-and state-dependent strength. Tectonophysics 211 (1), 115–134. http://dx.doi.org/10.1016/0040-1951(92)90055-B.

Dieterich, J.H., Smith, D.E., 2009. Nonplanar faults: Mechanics of slip and off-fault damage. Pure Appl. Geophys. 166 (10–11), 1799–1815. http://dx.doi.org/10.1007/s00024-009-0517-y.

Dixon, T.H., Norabuena, E., Hotaling, L., 2003. Paleoseismology and Global Positioning System: Earthquake-cycle effects and geodetic versus geologic fault slip rates in the Eastern California shear zone. Geology 31 (1), 55–58.

Dragert, H., Wang, K., James, T.S., 2001. A silent slip event on the deeper Cascadia subduction interface. Science 292 (5521), 1525–1528.

Erickson, B., Jiang, J., Barall, M., Lapusta, N., Dunham, E.M., Harris, R., Abrahams, L., Allison, K., Ampuero, J.-P., Barbot, S., Cattania, C., Elbanna, A., Fialko, Y., Idini, B., Kozdon, J., Lambert, V., Liu, Y., Luo, Y., Ma, X., Mckay, M.B., Segall, P., Shi, P., van den Ende, M., Wei, M., 2019. The Community Code Verification Exercise for Simulating Sequences of Earthquakes and Aseismic Slip (SEAS). Preprint, EarthArXiv, http://dx.doi.org/10.31223/osf.io/2dmp5.

Fialko, Y., Sandwell, D., Simons, M., Rosen, P.A., 2005. Three-dimensional deformation caused by the Bam, Iran, earthquake and the origin of shallow slip deficit. Nature 435 (7040), 295–299. http://dx.doi.org/10.1038/nature03425.

Fukuda, J., Miyazaki, S., Higuchi, T., Kato, T., 2008. Geodetic inversion for space-time distribution of fault slip with time-varying smoothing regularization. Geophys. J. Int. 173 (1), 25–48. http://dx.doi.org/10.1111/j.1365-246X.2007.03722.x.

Gaul, L., Kögl, M., Wagner, M., 2013. Boundary Element Methods for Engineers and Scientists: An Introductory Course with Advanced Topics. Springer Science & Business Media.

Heki, K., Miyazaki, S., Tsuji, H., 1997. Silent fault slip following an interplate thrust earthquake at the Japan trench. Nature 386, 595–597.

Hirose, H., Hirahara, K., Kimata, F., Fuiji, N., Miyazaki, S., 1999. A slow thrust slip event following the two 1996 Hyuganada earthquakes beneath the Bungo Channel, Southwest Japan. Geophys. Res. Lett. 26 (21), 3237–3240.

Hondros, G., 1959. The evaluation of Poisson's ratio and the modulus of materials of low tensile resistance by the Brazilian (indirect tensile) test with particular reference to concrete. Aust. J. Appl. Sci. 10 (3), 243–268.

Jeyakumaran, M., Rudnicki, J.W., Keer, L.M., 1992. Modeling slip zones with triangular dislocation elements. Bull. Seismol. Soc. Am. 82 (5), 2153–2169.

Johnson, K.M., 2018. Growth of fault-cored anticlines by flexural slip folding: analysis by Boundary Element Modeling. J. Geophys. Res. [Solid Earth] 123 (3), 2426–2447. http://dx.doi.org/10.1002/2017JB014867.

Johnson, K.M., Tebo, D., 2018. Capturing 50 Years of postseismic mantle flow at Nankai Subduction Zone. J. Geophys. Res. [Solid Earth] 123 (11), 10,091–10,106. http://dx.doi.org/10.1029/2018JB016345.

Li, D., Liu, Y., 2017. Modeling slow-slip segmentation in Cascadia subduction zone constrained by tremor locations and gravity anomalies. J. Geophys. Res.: Solid Earth 122 (4), 3138–3157. http://dx.doi.org/10.1002/2016JB013778.

Liu, Y., 2013. Numerical simulations on megathrust rupture stabilized under strong dilatancy strengthening in Slow Slip Region. Geophys. Res. Lett. 40 (7), 1311–1316. http://dx.doi.org/10.1002/grl.50298.

Liu, Y., Rice, J.R., 2005. Aseismic slip transients emerge spontaneously in three-dimensional rate and state modeling of subduction earthquake sequences. J. Geophys. Res.: Solid Earth 110 (B8), http://dx.doi.org/10.1029/2004JB003424.

Maerten, F., Resor, P., Pollard, D.D., Maerten, L., 2005. Inverting for slip on three-dimensional fault surfaces using angular dislocations. Bull. Seismol. Soc. Am. 95 (5), 1654–1665. http://dx.doi.org/10.1785/0120030181.

Martel, S.J., Muller, J.R., 2000. A two-dimensional boundary element method for calculating elastic gravitational stresses in Slopes. Pure Appl. Geophys. 157 (6), 989–1007. http://dx.doi.org/10.1007/s000240050014.

McCaffrey, R., 1992. Oblique plate convergence, slip vectors, and forearc deformation. J. Geophys. Res. 97 (B6), 8905–8915.

Meade, B.J., 2007. Algorithms for the calculation of exact displacements, strains, and stresses for triangular dislocation elements in a uniform elastic half space. Comput. Geosci. 33, 1064–1075. http://dx.doi.org/10.1016/j.cageo.2006.12.003.

Moon, S., Perron, J.T., Martel, S.J., Holbrook, W.S., St. Clair, J., 2017. A model of three-dimensional topographic stresses with implications for bedrock fractures, surface processes, and landscape evolution. J. Geophys. Res.: Earth Surf. 122 (4), 823–846. http://dx.doi.org/10.1002/2016JF004155.

Murray, J.R., Segall, P., Cervelli, P., Prescott, W., Svarc, J., 2001. Inversion of GPS data for spatially variable slip-rate on the San Andreas Fault near Parkfield, CA. Geophys. Res. Lett. 28 (2), 359–362.

Nikkhoo, M., Walter, T.R., 2015. Triangular dislocation: An analytical, artefact-free solution. Geophys. J. Int. 201 (2), 1119–1141. http://dx.doi.org/10.1093/gji/ggv035.

Okada, Y., 1985. Surface deformation due to shear and tensile faults in a half-space. Bull. Seismol. Soc. Am. 75 (4), 1135–1154.

Okada, Y., 1992. Internal deformation due to shear and tensile faults in a half-space. Bull. Seismol. Soc. Am. 82 (2), 1018–1040.

Ozawa, S., Nishimura, T., Suito, H., Kobayashi, T., Tobita, M., Imakiire, T., 2011. Coseismic and Postseismic Slip of the 2011 Magnitude-9 Tohoku-Oki Earthquake. Nature 475 (7356), 373–376. http://dx.doi.org/10.1038/nature10227.

Pape, D.A., Banerjee, P.K., 1987. Treatment of body forces in 2D elastostatic BEM using particular integrals. J. Appl. Mech. 54 (4), 866–871. http://dx.doi.org/10.1115/1.3173130.

Portela, A., Aliabadi, M.H., Rooke, D.P., 1992. The dual boundary element method: Effective implementation for crack problems. Internat. J. Numer. Methods Engrg. 33 (6), 1269–1287. http://dx.doi.org/10.1002/nme.1620330611.

Pritchard, M.E., Simons, M., Rosen, P.A., Hensley, S., Webb, F.H., 2002. Co-seismic slip from the 1995 July 30 M_w=8.1 Antofagasta, Chile Earthquake as constrained by InSAR and GPS observations. Geophys. J. Int. 150, 362–376. http://dx.doi.org/10.1046/j.1365-246X.2002.01661.x.

Rizzo, F., Shippy, D., 1977. An advanced boundary integral equation method for three-dimensional thermoelasticity. Internat. J. Numer. Methods Engrg. 11 (11), 1753–1768.

Segall, P., 2010. Earthquake and Volcano Deformation. Princeton University Press.

Thomas, A.L., 1993. Poly3D: A Three-Dimensional, Polygonal Element, Displacement Discontinuity Boundary Element Computer Program with Applications to Fractures, Faults, and Cavities in the Earth's Crust (M.S. thesis). Stanford University, Stanford, CA.

Vigny, C., Simons, W.J.F., Abu, S., Bamphenyu, R., Satirapod, C., Choosakul, N., Subarya, C., Socquet, A., Omar, K., Abidin, H.Z., Ambrosius, B.A.C., 2005. Insight into the 2004 Sumatra-Andaman earthquake from GPS measurements in Southeast Asia. Nature 436 (7048), 201–206.

Wei, M., Kaneko, Y., Liu, Y., McGuire, J.J., 2013. Episodic fault creep events in California controlled by shallow frictional heterogeneity. Nat. Geosci. 6 (7), 566–570. http://dx.doi.org/10.1038/ngeo1835.